Available online at www.sciencedirect.com
SCIENCE DIRECT®
Journal of Power Sources 154 (2005) 153–170
JOURNAL OF POWER SOURCES
www.elsevier.com/locate/jpowsour

Transfer function analysis of the dynamic behaviour of DMFCs: Response to step changes in cell current

U. Krewer[a], K. Sundmacher[a,b,*]

[a] *Max-Planck-Institut (MPI) für Dynamik Komplexer Technischer Systeme, Sandtorstraße 1, 39106 Magdeburg, Germany*
[b] *Otto-von-Guericke-Universität Magdeburg, Lehrstuhl für Systemverfahrenstechnik, Universitätsplatz 2, 39106 Magdeburg, Germany*

Received 1 November 2004; received in revised form 23 March 2005; accepted 2 April 2005
Available online 23 June 2005

Abstract

This paper presents investigations on the dynamic behaviour of DMFCs. Experimental cell voltage responses to cell current step changes are investigated with transfer function analysis. The voltage response in most places shows significant overshooting behaviour (up to 80%) when applying cell current steps to the DMFC. Linear system analysis is applied to a set of dynamic models with different complexity, and a criterion for cell voltage overshooting is developed. In all models the dominating physico-chemical phenomenon is the transport of methanol through the membrane, causing cathodic overpotential overshooting. This is supported by experimental analysis. The proposed models and transfer functions are suitable for controller design.

Keywords: DMFC; System analysis; Transfer function; Reduced model; Transient response; Dynamic operation

1. Introduction

First direct methanol fuel cell (DMFC) systems are commercially available (e.g. from SmartFuelCell, Germany) after more than one decade of research. They are mainly designed for the use as mobile supplies of electrical power in the range of up to a few hundred Watts. Nonetheless, many problems related to the operation of DMFCs under realistic, i.e. dynamic, operating conditions have yet to be solved. Therefore, all available fuel cell systems currently use a large battery or supercapacitor system between electric load and DMFC to buffer dynamic load demands. Usually, the DMFC is operated at a moderate, constant electric load which is suitable for long-term performance. Thus, the DMFC provides for a high state of charge of the much larger battery system. To widen the market for the DMFC, though, further miniaturisation and lower system costs have to be achieved. Therefore, it is attractive to be able to operate the DMFC system reliably and effectively without such a buffer system, or at least with a much smaller one. This in turn requires a deeper understanding of the behaviour of the DMFC under realistic dynamic operating conditions, like changes in the cell current (i.e. the external load demand) and the methanol feed concentration (as one of the few controllable system variables). Reduced but realistic mathematical models can prove useful in understanding dynamic interactions between the main physical and chemical phenomena, and hence may act as a basis for improved cell, system and controller design.

In recent years, research has been conducted on experimental DMFC responses to dynamic changes in cell current [1–4]. In the two latter publications, the authors performed various cell current steps and waited for a few seconds until performing the next step. They also conducted gradual cell loading and unloading from or to OCV. In addition, they combined cell current steps and gradual loading and unloading to driving cycles. Such measurements proved useful for empirical one-step-ahead prediction models of DMFC stacks [2]. Nonetheless, the experiments are not ideal for analysis of processes occurring inside the fuel cell. For example, the observation time after a current step is mostly only 30 s.

* Corresponding author. Tel.: +49 391 6110 350; fax: +49 391 6110 353.
E-mail address: sundmacher@mpi-magdeburg.mpg.de (K. Sundmacher).

0378-7753/$ – see front matter © 2005 Elsevier B.V. All rights reserved.
doi:10.1016/j.jpowsour.2005.04.006

Nomenclature

A	system matrix
A_s	geometric electrode area (26×10^{-4} m^2)
b_1, b_2	coefficients for the Laplace transformed flux
B	input matrix
c	concentration (mol m^{-3})
$c^{ref}_{CH_3OH}$	reference methanol concentration (1000 mol m^{-3})
$c^{M}_{H^+}$	proton concentration in membrane pores (1200 mol m^{-3}) [7]
C	output matrix
C^{AC}	anode double layer capacity (1827 C m^{-2}) (own CV measurements)
$C^{AC}_{CH_3OH}$	concentration variable in Laplace domain
C^{CC}	cathode double layer capacity (907 C m^{-2}) (own CV measurements)
D	direct transmission matrix
d^{AC}	thickness of anode catalyst layer (35×10^{-6} m) [10]
d^{AD}	thickness of anode diffusion layer (1.7×10^{-4} m) [10]
d^{M}	thickness of (fully hydrated) Nafion™ 105 membrane (10^{-4} m) [10]
D_{CH_3OH}	diffusion coefficient of methanol in water at 333 K (3.187×10^{-9} m^2 s^{-1}) (calc. acc. [24], p. 600)
$D^{M}_{CH_3OH}$	diffusion coefficient of methanol in membrane at 333 K (4.7×10^{-10} m^2 s^{-1}) (own measurements)
$D^{M}_{H^+}$	diffusion coefficient of protons in membrane (4.5×10^{-9} m^2 s^{-1}) [25]
F	Faraday constant (96485 C mol^{-1})
F^{A}	volume flow rate of anode feed (0.5 dm^3 min^{-1})
F_1,F_2 ($F_{1,rat}$,$F_{2,rat}$)	transcendental parts of the membrane transfer function (rational forms)
G	transfer function
i	counter
i_{cell}	cell current density (A m^{-2})
i_{max}	maximum initial cell current density for overshooting behaviour (A m^{-2})
I	current variable in Laplace domain
j	imaginary unit
k	constant in transfer function
k^{AD}	effective mass transport coefficient in anode diffusion layer ($D_{CH_3OH}(\epsilon^{AD})^{1.5}/d^{AD}$) (m s^{-1})
k_ϕ	electrokinetic permeability of membrane (1.13×10^{-19} m^2) [25]
$k_{\phi 2}$	electro-osmotic parameter (1.33×10^{-3} m^3 C^{-1}) (see text)
m	number of time-relevant singularities
n	number of poles and zeros
n_{CH_3OH}	flux density of methanol (mol m^{-2} s^{-1})
$n_{max,Pt}$	number of COx adsorption sites on Pt (0.11 mol CO m^{-2})
N_{CH_3OH}	variable of methanol flow in Laplace domain
P	pole of a transfer function
Pe	Peclet number ($k_{\phi 2} d^{M} i_{cell}/D^{M}_{CH_3OH}$)
$r_{A1}(r_{A10})$	reaction rate (constant) for anodic methanol oxidation (mol m^{-2} s^{-1})
$r_{A2}(r_{A20})$	reaction rate (constant) for anodic COx oxidation (mol m^{-2} s^{-1})
$r_C(r_{C0})$	reaction rate (constant) for cathodic reaction (0.5×10^{-4} mol m^{-2} s^{-1})
R	universal gas constant (8.314 J mol^{-1} K^{-1})
R_{el}	Ohmic resistance of the membrane (d_m/κ_m) (Ω m^2)
res	residue
s	Laplace variable
t	time (s)
T	cell temperature (333 K)
$u(U)$	input variable (in Laplace domain)
U^{θ}_0	standard cell voltage (1.213 V) (thermodynamic calculation)
U_{cell}	cell voltage (V)
V^{AC}	volume of anode catalyst layer (7.37×10^{-8} m^3)
w^{AC}	anode (and cathode) catalyst loading (5 mg cm^{-2})
$x(X)$	state variable (in Laplace domain)
$y(Y)$	output variable (in Laplace domain)
z	spatial coordinate in membrane (m)
Z	zero of a transfer function

Greek letters

α_{A1}, α_{A2}	charge transfer coefficient for anodic reactions (0.5)
α_C	charge transfer coefficient for cathodic reaction (0.5)
ϵ^{AC}	porosity of anode catalyst layer (0.81) [10]
ϵ^{AD}	porosity of anode diffusion layer (0.71) [10]
ϵ^{M}	porosity of membrane (0.4) [10]
η	electrode overpotential (V)
κ^{M}	ionic conductivity of membrane (0.0873 Ω^{-1} m^{-1}) (calc. acc. [12])
θ^{ref}_{COx}	reference COx surface coverage of active sites of Pt catalyst (0.5)
θ_{COx}	COx surface coverage of active sites of Pt catalyst
μ	pore fluid viscosity in membrane (4.823 kg m^{-1} s^{-1}) (calc. acc. [24], p. 441, 455)
ρ	radius in complex plane

Subscripts

A	anode
AC	anode catalyst layer

AE	anodic overpotential
AT	surface coverage
C	cathode
CH_3OH	methanol
COx	adsorbed intermediates occurring during methanol oxidation, e.g. CO, COH, CHO
num	numerically evaluated
rel	relative
ss	at steady state conditions prior to current step
tot	total

Superscripts

A	anode compartment
AC	anode catalyst layer
AD	anode diffusion layer
CC	cathode catalyst layer
M	membrane
M, A/(M, C)	boundary membrane–anode/ (membrane–cathode)

This time-span is sufficient for the above mentioned one-step-ahead models, but it is not sufficient for reaching a steady state for all dynamic variables.

This publication presents a systematic approach towards recording and analysing the DMFC voltage responses to load steps between two steady states. First, a polarisation curve is recorded, and the characteristic operating regimes (e.g. pseudo-ohmic regime) are identified. This is followed by various current steps between the identified regimes. The voltage response is recorded for 600 s. A subsequent analysis shows the characteristic influence of the operating regimes on the cell response.

Furthermore, mathematical models of different complexity are formulated and evaluated using the experimental data. A variety of models for different fuel cell types exists in literature, most are steady state models. Dynamic models are published e.g. by Heidebrecht and Sundmacher [5] (MCFC), Ceraolo et al. [6] (PEMFC), Sundmacher et al. [7] (DMFC), and Yerramalla et al. [8] (PEMFC).

Only few groups investigate on the dynamics of the DMFC. Besides empirical dynamic DMFC models, e.g. [2], the dynamic behaviour of DMFCs to concentration changes was modelled [7,9]. Zhou et al. [9] were among the first to apply system theoretical approaches on fuel cell models, and in particular on a DMFC model. They showed that non-minimal-phase behaviour, which was observed in a concentration step experiment, can be predicted via analysis of the transfer function of a respective linearised model. Linear system analysis has many advantages: analytical analysis of models can be conducted which may yield principle understanding of the influence of the underlying physico-chemical phenomena. Furthermore, transfer functions are a basis for controller design. Controllers based on physico-chemical process models are of particular interest.

In the following, dynamic DMFC models will be presented which analyse DMFC responses to dynamic load changes by using classical methods of system analysis. It will be shown that the applied methods predict conditions for experimentally observed overshooting behaviour. Additionally, the influence of reaction, methanol crossover and double layer charging will be investigated.

The presented models hold for analysis of an operating regime in which mass transport influences are minimised: low anodic residence time (i.e. negligible methanol concentration distribution), low current densities (i.e. negligible CO_2 bubble influence). This allows a much more indepth analysis of the processes occurring inside the MEA. Future works will systematically add outer influences like mass transport phenomena and a refined methanol oxidation mechanism.

2. Experimental setup

2.1. Applied DMFC design and materials

The experiments were carried out using a single DMFC fed with air and liquid methanol/water solutions [10]. The identical anode and cathode monopolar plates are made from graphite material (thickness 7 mm, material code FU4369) supplied by Schunk Kohlenstofftechnik (Germany). The necessary flow field structures for the reactant distribution over the MEA surface are millcut into the plates. They consist of parallel channels of 2 mm width and 2 mm depth, with 1 mm wide ribs between them. A distributor and collector channel connect the parallel channels to the inlet and outlet ports, respectively. The media (air and methanol/water solution) are supplied in one corner of the rectangular flow field and leave at the opposite corner. The flow field itself has the outer dimensions 65 mm × 40 mm, identical to the catalyst layer on the MEAs, which leads to an active area of $A_s = 26\,cm^2$.

As diffusion layer PTFE-coated TORAY carbon paper (TGP-H-060) is used, with a PTFE loading between 20 and 25 mass% with respect to the uncoated material.

Finally, the membrane electrode assemblies (MEA) are prepared from NAFION™ N-105 membrane foil, onto which the catalyst layers are applied using an airbrush technique developed by ZSW, Ulm (Germany) [11]. The anode catalyst layer features a catalyst loading of $5\,mg\,cm^{-2}$ (unsupported) platinum ruthenium black (Alfa Aesar Johnson Matthey HiSPEC™ 6000) and a NAFION™ content of 15 mass% relative to the metal loading (i.e. $0.75\,mg\,cm^{-2}$). The cathode catalyst layer has the same metal loading, but as catalyst (unsupported) pure platinum black is used (Alfa Aesar Johnson Matthey HiSPEC™ 1000) and the NAFION™ content is 10 mass% relative to the metal loading (i.e. $0.5\,mg\,cm^{-2}$).

The DMFC is completed by gold-plated copper plates as current collectors and stainless steel plates for bracing the whole sandwich structure. A torque of 5 Nm is exerted on the screws, which hold together the steel back plates. After assembly, each DMFC is conditioned and evaluated

by operation with pure humidified hydrogen and air for 3× 8 h, before it is operated on methanol solutions.

2.1.1. DMFC miniplant

For full-scale testing of DMFCs, a miniplant was designed by Schultz [10], which is fully automated (process control system PC-S7/WinCC by Siemens) to enable automatic testing procedures, with a special focus on dynamic operation. Fig. 1 shows a simplified flowsheet of the miniplant.

The DMFC cathode is supplied with dry air (dew point ≈271 K) at flow rates between 0.4 and 5.0 scbm h^{-1} (mass flow controller F101, type Mass6020 by Buerkert AG, Germany) at cathode outlet pressures of ambient up to 5 bars absolute (10^5–5×10^5 Pa). The air is pre-heated in a plate heat exchanger (W101), air temperatures and pressures are measured at the cathode inlet and outlet. At the cathode outlet, also the relative humidity of the air is measured (Q202, type HygroClip IE by rotronic AG, Switzerland). Finally the cathode exhaust air enters a condensor, where it is dried to reach a dew point below 263 K (condensate is collected). The dry air is sent into a fume hood, while its oxygen and carbon dioxide contents are measured. The oxygen sensor (Q204) is a paramagnetic sensor (PAROX 1000 H by MBE AG, Switzerland), while carbon dioxide is measured using an IR-sensor (Q203, type OEM-NDIR EGC-5% by Pewatron AG, Switzerland).

On the DMFC anode side, a liquid recycle loop is installed. It consists of two alternative cycles, one for methanol/water solution and one for pure water. The purpose of this is to enable a pulsed periodic operation of the DMFC, where the anode feed is changed stepwise between methanol/water solution and pure water automatically. Both branches of the anode cycle feature vessels for pressure equilibration and carbon dioxide removal (B1 and B2), gear pumps (P401 and P402) and heat exchangers (W403 and W406). Flow rates between 0.3 and 5 dm^3 min^{-1} can be achieved. Automatic valves (V403/V404 and V408/V409) enable a flexible and practically immediate change between methanol/water solution and pure water anode feed without causing significant disturbances in liquid flow rate and pressure. The flow rate is measured by a Coriolis-type sensor (F401, type MASS 2100 DI6

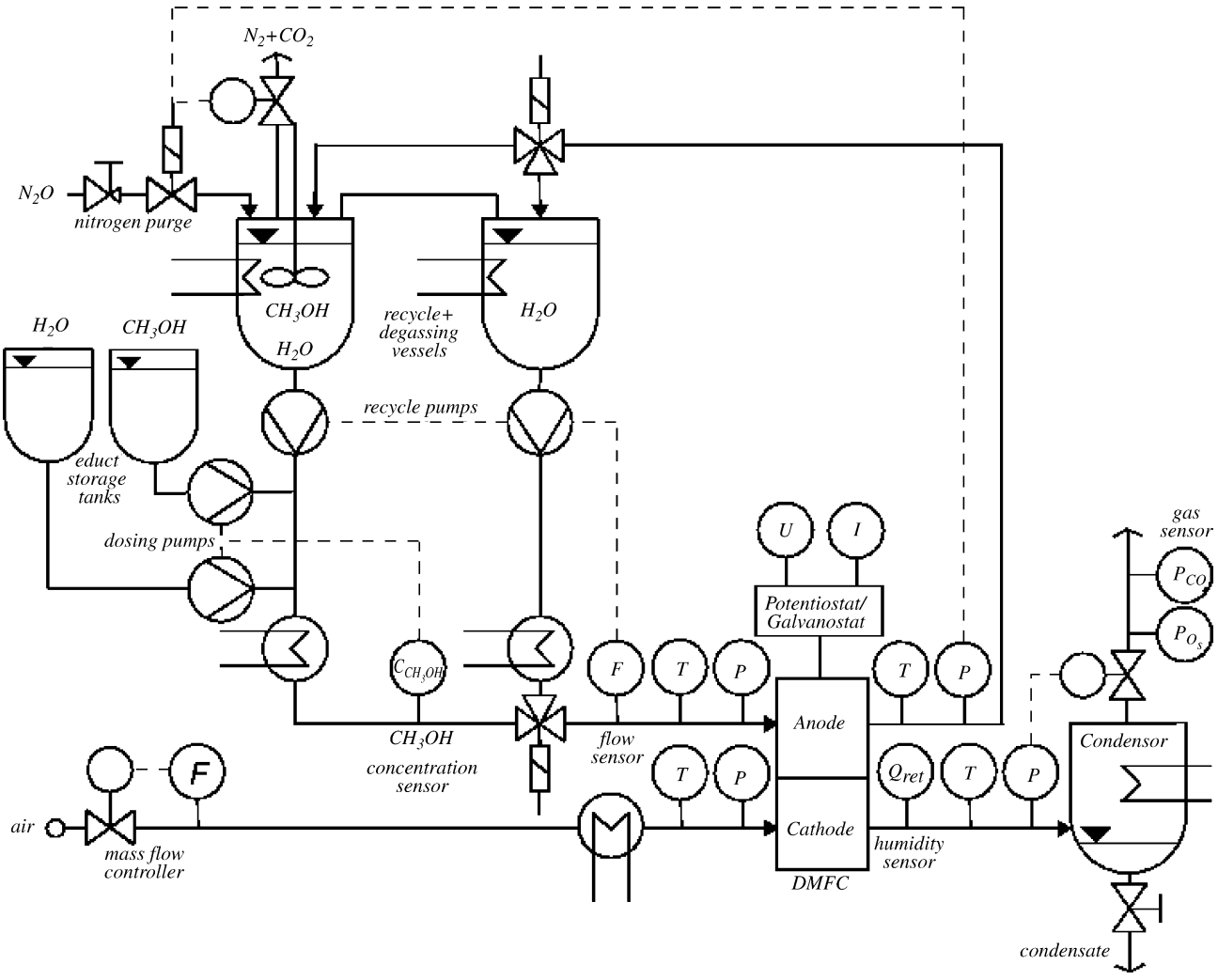

Fig. 1. Simplified flow scheme of DMFC miniplant with all important sensors and actuators.

by Danfoss, Denmark). Like on the cathode side, the medium temperature and pressure are measured at the cell inlet and outlet. The methanol concentration of the anode inlet medium is measured online using an ultrasound sensor (Q401, type LiquiSonic30 by SensoTech, GmbH, Germany), based on the influence of methanol concentration on the speed of sound in methanol/water solutions. This sensor is used in a methanol concentration controller, which uses two dosing pumps for pure methanol (P351) and pure water (P301) (mzr-2905 by HNP Mikrosysteme, Germany) as actuators. Methanol concentrations between zero and 1.5 mol dm^{-3} can be detected and controlled. The flow rates of the dosing pumps can be controlled in the range from 0.2 up to 18 cm^3 min^{-1}. To adjust the anode pressure and also to strip off carbon dioxide, the recycle vessels are equipped with a nitrogen purge/blanket. The anode pressure can be controlled in the range between ambient and 5 bars absolute (1.5×10^5 Pa). The liquid inlet temperature (which is also the DMFC temperature due to the applied high flow rates) can be controlled in the range between 253 and 423 K. The DMFC is electrically connected to a potentiostat (HP60-50 by Wenking GmbH, Germany), which enables operation of fuel cells from below 1 W up to 1 kW at a maximum of 50 A. Galvanostatic as well as potentiostatic operation is possible, with the option to automatically run user-defined load scenarios.

The array of sensors around the DMFC enables full online material balancing of all key components (oxygen, methanol, water, carbon dioxide).

3. Step changes in cell current

3.1. Experimental

First, a steady state polarisation curve was recorded with the following operating conditions:

- Anode:
  - feed temperature: 333 K (equals whole DMFC temperature),
  - methanol feed concentration: 1 mol dm^{-3},
  - flow rate: 0.5 dm^3 min^{-1},
  - pressure: 1.7 bar;
- Cathode:
  - feed temperature: 293 K,
  - feed composition: dry air (dew point ≈271 K),
  - flow rate: 0.5 scbm h^{-1},
  - pressure: 1.7 bar.

As can be seen in Fig. 2, the OCV lies around 0.6 V, and the limiting current density is approximately 200 A m^{-2}. The fairly low OCV can be attributed to the crossover of methanol and is in accordance with literature data (0.65 V in [7], 0.55–0.7 V in [12]).

At temperatures up to 333 K, it is known that methanol chemisorption only occurs on Pt and water adsorption on Ru, respectively. This mechanism changes when going to higher temperatures. Then, methanol is also oxidised on Ru (see [13]). In addition, methanol oxidation accelerates with higher temperatures. Since the aim of this publication is the development and investigation of dynamic DMFC models, defined conditions and reaction mechanisms for modelling are mandatory for obtaining reasonable results. Hence, an operating temperature of 333 K was chosen. The relatively low performance of the presented DMFC mainly results from this moderate operating temperature.

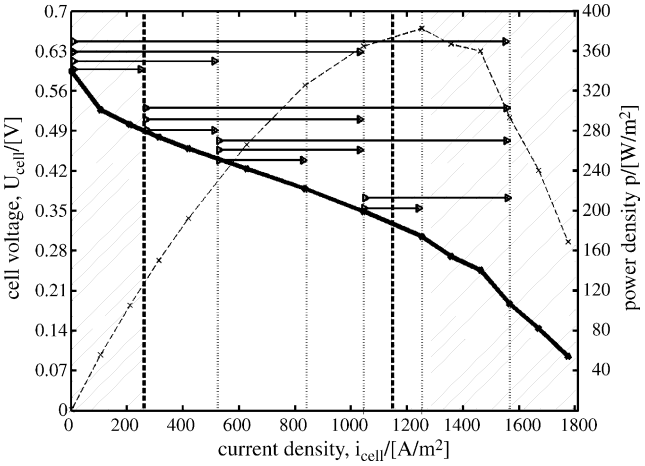

Fig. 2. Recorded polarisation curve with illustration of conducted current steps (arrows) and the activation-dominated regime (hatched area, left), pseudo-ohmic regime (middle) and transport-controlled regime (hatched area, right).

In the polarisation curve (Fig. 2), the activation-controlled and mass-transport controlled regimes are marked by hatching. In between, without hatching, is the pseudo-ohmic regime. When investigating cell responses to current steps, the initial current as well as the final current should strongly influence the voltage response. Hence, a series of current steps between the different regimes were performed. These steps are visualised by arrows in Fig. 2. Figs. 3–5 show voltage responses to the different current steps. Each of the current densities was maintained for 10 min before it was again set to the previous current level. This assures that the cell reaches a steady state before the next current change is applied. Voltage responses of systems which are not in steady state prior to the current step do not have defined conditions, and interpretation and modelling would be difficult.

Fig. 3 shows voltage responses to steps below 520 A m^{-2}. The solid line shows cell voltage responses to current density steps between 520 and 260 A m^{-2}. The voltage response is quite symmetrical, showing instantaneous relative overshoots of approximately 40% whenever the current is switched between the levels, i.e. the absolute value of the voltage change directly after the current step exceeds the absolute steady state voltage difference by 40%. The steady state is reached after a certain relaxation time. In contrast to this, voltage responses to current density steps between 0 A m^{-2}, i.e. open circuit voltage (OCV), and 520 A m^{-2} are non-symmetrical. The

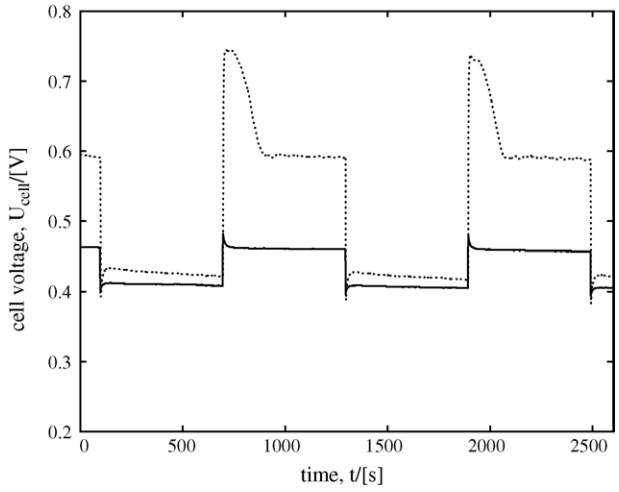

Fig. 3. Cell voltage as a function of time for current steps from the lower pseudo-ohmic regime: Current steps between 0 and 520 A m^{-2} (dotted), steps between 260 and 520 A m^{-2} (solid).

voltage response at OCV, i.e. when the current is switched off, shows an overshoot of approximately 80%, and a relaxation time of up to 250 s, in comparison to roughly 50 s in the formerly discussed current steps. Additionally, the shape of the OCV voltage response shows rather S-shape than exponential behaviour (like in the former step). At a current density of 260 A m^{-2} the activation-controlled regime is reached and the forward reaction, i.e. the oxidation of methanol takes place. At OCV the overall reaction stops immediately, and an equilibrium which is not clearly defined is reached. This equilibrium depends on the oxidation state of the catalyst as well as on the equilibria between the various methanol reaction intermediates. This process takes much more time than reaching a steady state at electric current.

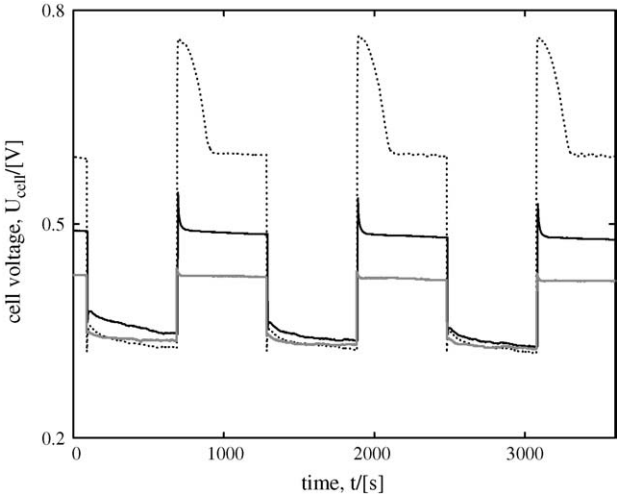

Fig. 4. Cell voltage as a function of time for current steps from the upper pseudo-ohmic regime: Current steps between 0 and 1050 A m^{-2} (dotted), steps between 260 and 1050 A m^{-2} (black), steps between 520 and 1050 A m^{-2} (grey).

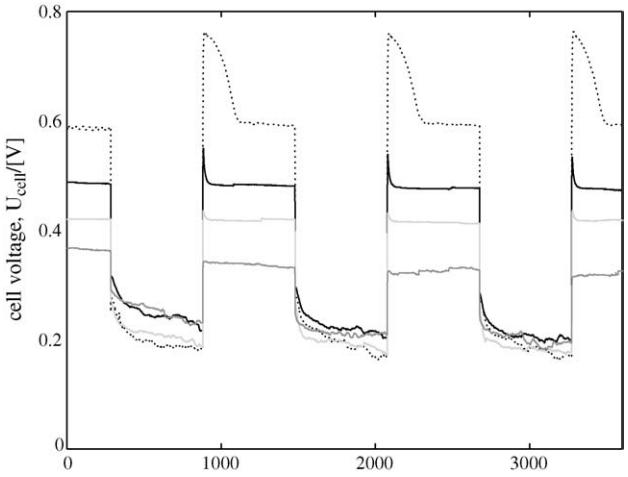

Fig. 5. Cell voltage as a function of time for current steps from the mass-transport controlled regime: Current steps between 0 and 1570 A m^{-2} (dotted), steps between 260 and 1570 A m^{-2} (black, solid), steps between 520 and 1570 A m^{-2} (light grey), steps between 1050 and 1570 A m^{-2} (dark grey).

Similar effects can be observed for steps from higher current density levels, see Figs. 4 and 5. Steps to OCV result in much higher overshooting and longer relaxation times. In contrast to Fig. 3, voltage responses to a current step-up show small fluctuations. Furthermore, the voltage overshoots and subsequently decays to new quasi-steady state levels. These new quasi-steady state voltages may be as low as the overshoot voltages obtained directly after the current step. Decay and fluctuation should be assigned to diffusion limitation effects. While the upper current density in Fig. 4 is always 1050 A m^{-2}, which is close to the mass transport dominated regime but not within, the upper current density in Fig. 5 is well within this region. This leads to the following: While the voltage response to the current step-up in Fig. 4 is decaying to a steady state cell voltage near the overshoot cell voltage due to mass transport limitation effects, Fig. 5 shows intense fluctuations of the voltage signal, attributed additionally to the onset of CO_2 bubble formation. Furthermore, it can be observed that the system takes in the order of minutes to reach a new steady state, if at all in the given time interval. Apart from these effects, when stepping down to lower currents, Figs. 4 and 5 show smooth voltage responses with exponential shapes after the overshoots. This behaviour is comparable to the current density steps from 520 to 260 A m^{-2} in Fig. 3.

Fig. 6 plots the absolute overshoots of cell voltage responses vs. the initial and final cell current density for the conducted current steps. Only stable voltage signals are evaluated. As can be seen, increasing final cell current density correlates with decreasing absolute overshoot (for constant initial cell current density). An already mentioned reason for this kind of behaviour is the decay of cell voltage to a lower steady state voltage after an overshoot, which can be attributed to mass transport phenomena.

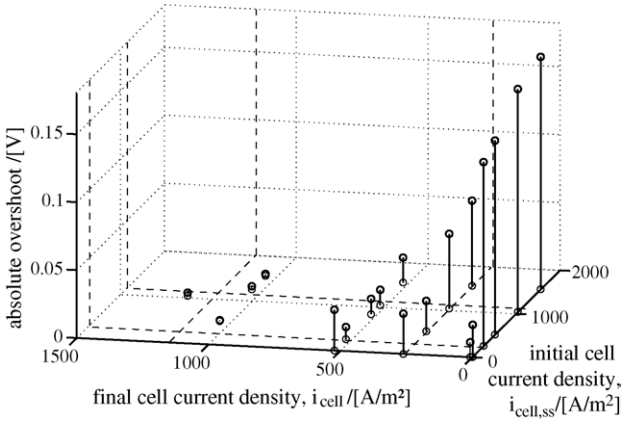

Fig. 6. Voltage response to cell current steps: Absolute overshoot vs. initial and final cell current density (only stable voltage signals were evaluated, dashed lines separate the regimes in the polarisation curve, compare with Fig. 2).

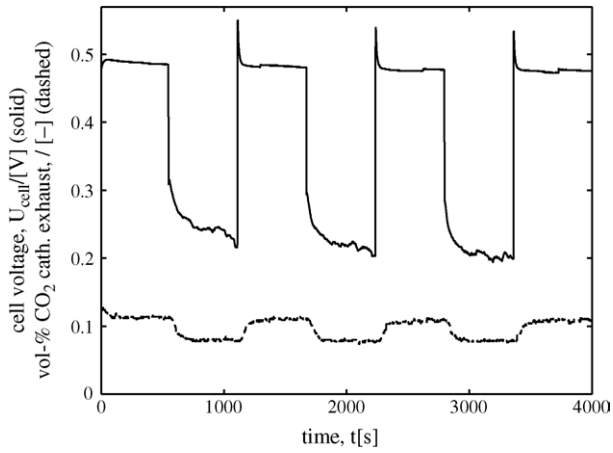

Fig. 7. Cell voltage (solid) and CO_2 content in cathode exhaust air (dashed) as a function of time for current steps between 260 and 1050 A m^{-2}.

Furthermore, except for current density steps from 0 A m^{-2} to higher current densities, higher initial cell current densities result in higher overshoots (for constant final cell current density). This leads to the following effect: the final steady state cell voltage is mostly independent from the initial cell current density. Hence, the cell voltage, the methanol concentration on anode and cathode side, and the methanol crossover should reach the same steady state after a current step to the same final cell current density. In contrast to this, the initial conditions vary strongly. Directly after the current step, the cell voltage is strongly influenced by the initial steady state and methanol crossover. Methanol crossover will be lower with increasing initial cell current density. This may cause lower cathodic overpotentials, and as a result a higher cell voltage, when switching to the same final cell current density from higher initial cell current densities.

Since the methanol crossover is proportional to the CO_2 concentration on the cathode side, there is a dependence of the CO_2 concentration on current density. Schultz et al. [14,10] have shown this in steady state measurements and simulations. Due to online detection of CO_2 at the cathode outlet (after the condensor, see Fig. 1), the experimental setup enables dynamic recording of the CO_2 concentration. Fig. 7 presents the CO_2 content in the cathode exhaust air as a function of time for the current steps between 260 and 1050 A m^{-2}. Although the response cannot be quantitatively interpreted due to the residence time influence of the fixtures (pipes, condensor), Fig. 7 shows qualitatively the response of methanol crossover to the current steps: After a delay time of ~30 s, the CO_2 concentration gradually moves to a higher steady state when stepping down to 260 A m^{-2}, or to a lower steady state when stepping up to 1050 A m^{-2}. Here, a higher current density causes higher anodic methanol conversion. This lowers the anodic methanol concentration, hence the diffusive methanol crossover and the cathodic CO_2 production. The opposite holds for a decrease in current density.

3.2. System theoretical analysis of process models of different complexity

3.2.1. Set of governing equations

To describe and analyse the behaviour of the DMFC with respect to dynamic changes in current density, a non-linear mathematical model was developed accounting for the following phenomena (see Fig. 8):

- Diffusive mass transport through the anode diffusion layer.
- Electrochemical oxidation of methanol in the anode catalyst layer.
- Formation of an adsorbed intermediate COx during electrochemical methanol oxidation.
- Electrochemical reduction of oxygen in the cathode catalyst layer.
- Methanol crossover, i.e. undesired transfer of methanol through the PEM by diffusion and electroosmosis.
- Undesired electrochemical oxidation of methanol at the cathode catalyst layer.

The following model assumptions were made:

- Residence time in the anode compartment is very low, so that the compartment effectively is a differential reactor. Hence, the concentration in the compartment is assumed to be equal to the inlet concentration.
- Ohmic drops in current collectors and electric connections are negligible.
- The fuel cell is operated isothermally.
- Oxygen is fed in excess, i.e. oxygen conversion in the cathode compartment is negligible, and therefore no oxygen mass balance is required.
- Oxygen and carbon dioxide do not diffuse into the PEM.
- Water concentration is assumed to be constant (excess component in a liquid mixture).
- Mass transport resistances in the catalyst layers are negligible due to the fact that these are thin (35 μm) in comparison to the diffusion layer (170 μm) and the PEM (100 μm).

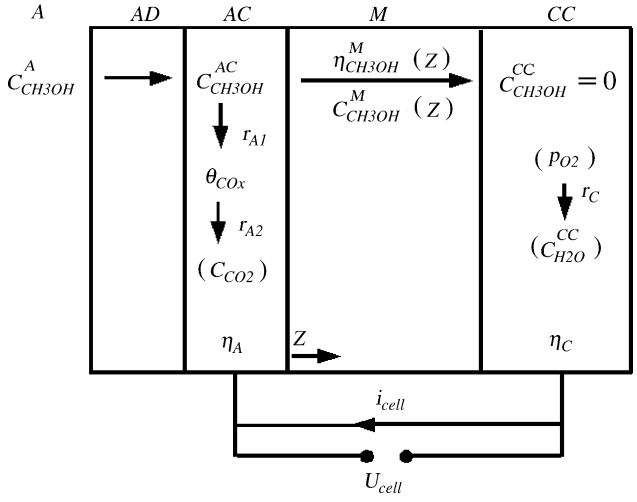

Fig. 8. Illustration of the DMFC model including reactants and physico-chemical phenomena (A: anode compartment; AD: anode diffusion layer; AC: anode catalyst layer; M: membrane; CC: cathode catalyst layer).

- Mass transport in the diffusion layers is quasi-steady state.
- On the anode side, a pure liquid phase mixture is assumed, i.e. gas-phase formation by release of carbon dioxide bubbles is not taken into account. Problems with bubble formation only get visible when working and modelling in or near the transport-controlled regime of the polarisation curve, which is not done here.
- Methanol which is transported to the cathode is assumed to be instantaneously reacting with oxygen at the cathode, hence its concentration in the cathode catalyst layer is zero.
- Experiments were carried out with zero pressure difference between anode and cathode compartment, hence no pressure-driven transport through the membrane takes place.
- In the modelled scenarios, all reactions are far from equilibrium. Hence, Tafel kinetics are used for description.
- Due to the postulated instantaneous dissolution of carbon dioxide after production and due to the applied Tafel kinetics, no carbon dioxide balance is formulated.
- A two step reaction mechanism is used to describe the electrochemical oxidation of methanol at the platinum–ruthenium catalyst. The mechanism is a lumped approach and accounts for the oxidation of a Pt-adsorbed intermediate COx (e.g. CO):

$$CH_3OH + Pt \rightarrow Pt\text{-}COx + 4H^+ + 4\,e^- \quad (1)$$

$$Pt - COx + H_2O \xrightarrow{Ru} CO_2 + 2H^+ + 2\,e^- + Pt \quad (2)$$

There is intense discussion about the real methanol oxidation mechanism and the intermediates involved, see [15–19]. Focus of this work is not on determining or validating a specific reaction mechanism. Instead the fact is used that methanol oxidation is known to occur via a carbon intermediate which is adsorbed on active Pt surface sites and which tends to block the sites. As this intermediate may be CO, COH, CHO or other postulated and measured species, the lumped intermediate COx is introduced. While the first reaction step is the reaction of methanol to the intermediate, the second reaction is the oxidation of this intermediate plus an integrated reaction, which is the adsorption of water on Ru. This adsorption step on Ru is known to be fast compared to the slow methanol oxidation, see [20], and therefore it is assumed to be in equilibrium.

As can be seen from the assumptions, the model is limited to an operating regime of very high anodic volume flow, a lumped reaction mechanism and the lower pseudo-ohmic regime of the polarisation curve. Under these conditions, an analysis of the dynamic processes occurring inside the MEA can be conducted with minimal influence of mass transport.

Based on the assumptions given above, balance equations for methanol concentration in the catalyst layer (Eq. (3)), COx surface coverage (Eq. (4)), methanol concentration in the membrane (Eq. (6)), anodic overpotential (Eq. (5)) and cathodic overpotential (Eq. (7)), as well as reaction rates (Eqs. (8)–(10)) were formulated:

$$\frac{dc^{AC}_{CH_3OH}}{dt} = \frac{k^{AD}A_s}{V^{AC}}(c^{A}_{CH_3OH} - c^{AC}_{CH_3OH}) - \frac{A_s}{V^{AC}}n^{M,A}_{CH_3OH} - \frac{A_s}{V^{AC}}r_{A1} \quad (3)$$

$$\frac{d\theta_{COx}}{dt} = \frac{1}{n_{max,Pt}}(r_{A1} - r_{A2}) \quad (4)$$

$$\frac{d\eta_A}{dt} = \frac{1}{C^{AC}}i_{cell} + \frac{1}{C^{AC}}(-4Fr_{A1} - 2Fr_{A2}) \quad (5)$$

$$\frac{\partial c^{M}_{CH_3OH}}{\partial t} = -\frac{\partial n^{M}_{CH_3OH}}{\partial z} \quad (6)$$

$$\frac{d\eta_C}{dt} = -\frac{1}{C^{CC}}i_{cell} - \frac{1}{C^{CC}}(6Fr_C + 6Fn^{M,C}_{CH_3OH}) \quad (7)$$

$$r_{A1} = r_{A10}\frac{c^{AC}_{CH_3OH}}{c^{ref}_{CH_3OH}}\frac{1-\theta_{COx}}{1-\theta^{ref}_{COx}}\exp\left\{\frac{\alpha_{A1}F}{RT}\eta_A\right\} \quad (8)$$

$$r_{A2} = r_{A20}\frac{\theta_{COx}}{\theta^{ref}_{COx}}\exp\left\{\frac{\alpha_{A2}F}{RT}\eta_A\right\} \quad (9)$$

$$r_C = -r_{C0}\exp\left\{\frac{-(1-\alpha_C)F}{RT}\eta_C\right\} \quad (10)$$

$$n^{M}_{CH_3OH} = -D^{M}_{CH_3OH}\frac{\partial c^{M}_{CH_3OH}}{\partial z} + c^{M}_{CH_3OH}k_{\phi 2}i_{cell} \quad (11)$$

$$U_{cell} = U^{\theta}_0 - \eta_A + \eta_C - \frac{d^M}{\kappa^M}i_{cell} \quad (12)$$

Transport of methanol through the membrane is described by Eq. (11), consisting of a Fickian diffusion term (first term on r.h.s.), and an electroosmotic term (second term) with the lumped electroosmotic parameter $k_{\phi 2}$. The latter is derived by using the isobaric convective flow velocity equation given

by Schloegl [21]:

$$n^{\mathrm{M}}_{\mathrm{CH_3OH,convective}} = -c^{\mathrm{M}}_{\mathrm{CH_3OH}} \frac{k_\phi}{\mu} c^{\mathrm{M}}_{\mathrm{H^+}} F \frac{\mathrm{d}\phi}{\mathrm{d}z} \tag{13}$$

Analogous to Sundmacher et al. in [7], the electrostatic gradient $\mathrm{d}\phi/\mathrm{d}z$ can be formulated in terms of the cell current density i_{cell}, using the Nernst–Planck equation for proton transport:

$$\frac{\mathrm{d}\phi}{\mathrm{d}z} = -\frac{i_{\mathrm{cell}}}{c^{\mathrm{M}}_{\mathrm{H^+}} F^2 (D^{\mathrm{M}}_{\mathrm{H^+}}/RT + c^{\mathrm{M}}_{\mathrm{H^+}} k_\phi/\mu)} \tag{14}$$

which is inserted into Eq. (13). From this, a lumped electroosmotic parameter $k_{\phi 2}$ is obtained:

$$k_{\phi 2} = \frac{k_\phi}{\mu F (D^{\mathrm{M}}_{\mathrm{H^+}}/RT + c^{\mathrm{M}}_{\mathrm{H^+}} k_\phi/\mu)} \tag{15}$$

The overall cell voltage U_{cell} (Eq. (12)) is a function of the standard open-circuit cell voltage U^θ_0, the overpotentials at anode and cathode, η_{A} and η_{C}, respectively, and the Ohmic loss in the PEM, $R_{\mathrm{el}} = d^{\mathrm{M}}/\kappa^{\mathrm{M}}$. The overpotentials are defined with regard to the standard electrode potentials.

3.2.2. Linear system analysis and overshoot

After linearisation, the given set of balance equations. (3)–(7), can be cast into the following standardised state space form:

$$\frac{\mathrm{d}\mathbf{x}}{\mathrm{d}t} = A\mathbf{x}(t) + Bu(t) \tag{16}$$

$$y(t) = C\mathbf{x}(t) + Du(t) \tag{17}$$

where A, B, C and D are the system matrix, input matrix, output matrix and direct transmission matrix, respectively, u the perturbed input variable, i.e. in this case the cell current density, y the observed output variable, i.e. the cell voltage response, and $\mathbf{x}$ is the vector of state variables.

Laplace transformation ($t \to s; y(t) \to Y(s); u(t) \to U(s); \mathbf{x}(t) \to \mathbf{X}(s)$) of this equation set yields the transfer function G, which is the ratio of output to input variable:

$$G(s) = \frac{Y(s)}{U(s)} = B(sI - A)^{-1}C + D \tag{18}$$

$Y(s)$ is the Laplace transformed cell voltage, and $U(s)$ is the Laplace transformed cell current density. Instead of calculating the global transfer function using all equations at once, the system can be decomposed into single modules which are interconnected as shown in the blockdiagram in Fig. 9. This decomposition is done with regard to the different functional layers of the DMFC: Anode catalyst layer (G_{A}), cathode catalyst layer (G_{C}) and membrane (G_{M}). Subsequently, the anode catalyst layer is decomposed into the different state variables: Methanol concentration (G_{AC}), COx surface coverage (G_{AT}) and anode catalyst charge (G_{AE}). This method of decomposition has the advantage that the mathematical description of the single modules can be chosen from within a library. Besides the descriptions derived from Eqs. (3)–(12),

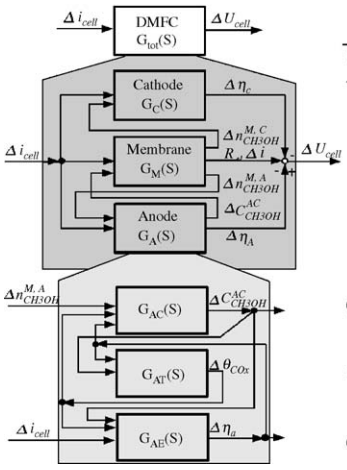

Fig. 9. Representation of the DMFC as a transfer function block diagram (left) and an overview of the presented model variants (right): $G = \mathrm{const} \Rightarrow$ quasi-steady state assumed.

this library contains various alternative mathematical descriptions for each state variable. The appropriate description has to be chosen according to the model variant. Four different model variants are investigated in the following chapters, an overview is given in Fig. 9 (r.h.s.).

The experimental input $u(t)$ shows a step in cell current density, which in the Laplace domain gives $U(s) = \Delta u/s$, where Δu is the step size $\Delta u = i_{\mathrm{cell},t>0} - i_{\mathrm{cell,ss}}$. The index ss always refers to the steady state prior to the current step.

Based on the observation that the experimental voltage responses typically overshoot directly after the current step, a criterion in the Laplace domain for overshooting is formulated: The transfer function $G(s)$ is written in the pole-zero form:

$$G(s) = k \frac{\prod_{i=1}^{n}(s - Z_i)}{\prod_{i=1}^{n}(s - P_i)} \tag{19}$$

where Z_i are the zeros or roots of the numerator polynomial and P_i are the poles, i.e. the roots of the denominator polynomial. The number of poles and zeros is the same, as soon as $D \neq 0$. As illustrated in Fig. 10, in case of overshooting, the system response has its maximum absolute value at $t \to 0^+$, i.e. $\lim_{t\to 0} |y(t)|$, and decreases for $t \to \infty$ towards a new steady state with a smaller absolute value, i.e. $\lim_{t\to\infty} |y(t)|$. Final value theorem and initial value theorem then result in

$$\lim_{t\to 0} y(t) = \lim_{s\to\infty} Y(s)s = \lim_{s\to\infty} G(s)\Delta u = k\Delta u \tag{20}$$

$$\lim_{t\to\infty} y(t) = \lim_{s\to 0} Y(s)s = \lim_{s\to 0} G(s)\Delta u = k\Delta u \frac{\prod_{i=1}^{n}(-Z_i)}{\prod_{i=1}^{n}(-P_i)} \tag{21}$$

And the condition:

$$\lim_{t\to 0} |y(t)| > \lim_{t\to\infty} |y(t)| \tag{22}$$

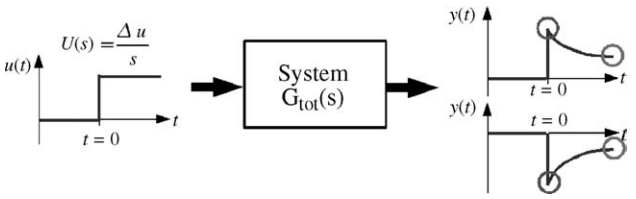

Fig. 10. Principle of overshooting systems.

gives the overshoot criterion:

$$\| \prod_{i=1}^{n} P_i \| > \| \prod_{i=1}^{n} Z_i \| \tag{23}$$

The following chapters investigate four model variants.

3.2.3. Reaction-model with one state variable (1x-model)

The given set of balance equations (3)–(7) represents different dynamic processes which interact with each other. To study and understand the model and the influences of the various phenomena, a study of the individual dynamic processes is helpful. A minimum dynamic model with one state variable, denoted in the following as 1*x*-model, is derived from the set of Eqs. (3)–(12). The most influential state variable is the methanol concentration in the catalyst layer: It is changing during a current step, influencing anode and cathode overpotential, as well as the methanol profile within the membrane. For the 1*x*-model the following assumptions are made:

- The balance equations for charge, Eqs. (5) and (7), and methanol inside the membrane, Eq. (6), are in a quasi-steady state.
- The balance equation for methanol inside the anode catalyst layer, Eq. (3), is the only dynamic equation.
- The methanol oxidation is assumed to take place without the reaction intermediate COx, therefore the rate expression r_{A1} has to be modified to match the overall reaction:

$$CH_3OH + H_2O \rightarrow CO_2 + 6H^+ + 6\,e^- \tag{24}$$

and

$$r_{A1} = r_{A10} \frac{c^{AC}_{CH_3OH}}{c^{ref}_{CH_3OH}} \exp\left\{ \frac{\alpha_{A1} F}{RT} \eta_A \right\} \tag{25}$$

Accordingly, the number of exchanged electrons in Eq. (5) has to be changed from 4 to 6, and Eq. (4) is dismissed.

Also, the description of mass transport through the membrane is simplified. The most simple mass transport model is a Fick diffusion approach, assuming a negligible electroosmotic drag, hence Eq. (11) reduces to

$$n^{M}_{CH_3OH} = \frac{D^{M}_{CH_3OH}}{d^M} c^{AC}_{CH_3OH} \tag{26}$$

This means that a linear concentration profile in the membrane is assumed, and thus the methanol flux density of methanol is constant all over the membrane:

$$n^{M,A}_{CH_3OH} = n^{M,C}_{CH_3OH} = n^{M}_{CH_3OH} \tag{27}$$

Fig. 9 (r.h.s.) gives an overview of the transfer functions for the 1*x*-model. Calculation yields the following transfer functions, where in- and outputs are in the same order, from top to bottom, as in the blockdiagram in Fig. 9 (l.h.s.):

$$G_C = \left(\frac{RT}{F(i_{cell,ss} + 6Fn^{M,C}_{CH_3OH,ss})(\alpha_C - 1)} \quad \frac{6RT}{(i_{cell,ss} + 6Fn^{M,C}_{CH_3OH,ss})(\alpha_C - 1)} \right) \tag{28}$$

$$G_M = \begin{pmatrix} 0 & D^{M}_{CH_3OH}/d^M \\ d^M/\kappa^M & 0 \\ 0 & D^{M}_{CH_3OH}/d^M \end{pmatrix} \tag{29}$$

$$G_{AC}(s) = \begin{pmatrix} \dfrac{-A_s/V^{AC}}{s + k^{AD}A_s/V^{AC} + A_s/V^{AC} r_{A10} \exp(\alpha_{A1} F \eta_{A,ss}/R/T)/c^{ref}_{CH_3OH}} \\ \dfrac{-A_s/V^{AC} r_{A10} \alpha_{A1} F/R/T \exp(\alpha_{A1} F \eta_{A,ss}/R/T) c^{AC}_{CH_3OH,ss}/c^{ref}_{CH_3OH}}{s + k^{AD}A_s/V^{AC} + A_s/V^{AC} r_{A10} \exp(\alpha_{A1} F \eta_{A,ss}/R/T)/c^{ref}_{CH_3OH}} \end{pmatrix}^T \tag{30}$$

$$G_{AE}(s) = \left(-\frac{RT}{\alpha_{A1} F c^{AC}_{CH_3OH,ss}} \quad \frac{RT}{\alpha_{A1} F i_{cell,ss}} \right) \tag{31}$$

Applying the overshoot criterion, Eq. (23), on the derived model equations results in the following overshoot criterion:

$$i_{cell,ss} < i_{max} = \frac{6FD^{M}_{CH_3OH} k^{AD} c^{AC}_{CH_3OH,ss} (\alpha_{A1} + \alpha_C - 1)}{d^M (k^{AD}(1 - \alpha_C) + k^M \alpha_{A1})} \tag{32}$$

Obviously, there is a maximum initial steady state current density i_{max}, above which in any case no overshooting, and below which always overshooting will occur. It should be emphasized that with such a simple model of only one state variable, the voltage response can already show overshoots depending on the parameters. In case that both charge transfer coefficients, α_{A1} and α_C, are 0.5, i_{max} is 0, therefore no overshoots can occur. Fig. 11 (top) shows the experimental cell voltage response for a current density step from 520 to 260 A m^{-2}. In order to simulate this, all known parameters (values see Nomenclature) are inserted in the model and the

charge transfer coefficients α_{A1} and α_C are set to 0.5 (standard value). Parameters unknown are the anodic and cathodic reaction rate constants, r_{A10} and r_{C0}, respectively. They are estimated according to the following criteria. First, the cathodic reaction should be much faster than the anodic reaction. Second, the experimentally observed polarisation curve (Fig. 2) has to be fitted. Accordingly, the cathodic reaction rate constant is chosen to be two orders higher than the anodic reaction rate constant, and the reaction parameters are adjusted to fit the experimental polarisation curve. Fig. 11 (bottom, dotted line) shows the simulated voltage response (reaction parameters are given ibidem). With this set of parameters, no overshooting can occur according to Eq. (32). The voltage response for charge transfer coefficients >0.5 is shown in Fig. 11 (bottom, solid line). As expected for the given parameter set, the voltage response shows overshooting ($i_{cell,ss} < i_{max}$). Qualitatively, the model's voltage response is similar to the experimental voltage response. Both have a maximum at $t = 0$ s and decrease slowly to the new steady state. Nonetheless, quantitative comparison shows significant differences. The model's absolute overshoot and the relaxation time are much smaller than the experimental values. The absolute overshoot, i.e. the difference between maximum voltage and new steady state voltage, is 20 mV in the experiment and approximately 10 times smaller in simulation. This may originate from the selected set of reaction parameters. The more important deviation is the relaxation time: while in the experiment it takes approximately 40–50 s to reach a new steady state, the steady state is reached within 5 s in the model. This indicates that the chosen storage capacity within the model is insufficient. As the only storage in the model is the anode catalyst layer volume which is given by cell geometry and the layers' morphology, other additional storages have to exist.

3.2.4. Reaction–adsorption model with two state variables (2x-model)

As the 1*x*-model cannot describe the experimental observations appropriately, the model is extended by introducing a second state variable θ_{COx}, hence another storage. As explained already in Section 3.2.1, it is known that the electrochemical methanol oxidation follows a multi-step mechanism including at least one adsorption step, e.g. like in Eqs. (1) and (2). The mass balance of the intermediate step is given in Eq. (4), with the reaction rates r_{A1} and r_{A2} as in Eqs. (8) and (9). The description of mass transfer through the membrane is identical to the one in the 1*x*-model. The new model will be referred to as 2*x*-model due to its two state variables.

As in the 1*x*-model, the equation system is transformed into Laplace domain. G_C and G_M are identical to the ones in the 1*x*-model. Due to the new state variable θ_{COx}, the transfer functions for the anode (in- and outputs are in the same order as in Fig. 9) change as follows:

$$G_{AC}(s) = \begin{pmatrix} \frac{-A_s/V^{AC}}{s+k^{AD}A_s/V^{AC}+A_s/V^{AC}r_{A10}\exp(\alpha_A F\eta_{A,ss}/R/T)/c^{ref}_{CH_3OH}(1-\theta_{COx,ss})/(1-\theta^{ref}_{COx})} \\ \frac{A_s/V^{AC}r_{A10}\exp(\alpha_A F\eta_{A,ss}/R/T)c^{AC}_{CH_3OH,ss}/c^{ref}_{CH_3OH}/(1-\theta^{ref}_{COx})}{s+k^{AD}A_s/V^{AC}+A_s/V^{AC}r_{A10}\exp(\alpha_A F\eta_{A,ss}/R/T)/c^{ref}_{CH_3OH}(1-\theta_{COx,ss})/(1-\theta^{ref}_{COx})} \\ \frac{-A_s/V^{AC}r_{A10}\alpha_A F/R/T\exp(\alpha_A F\eta_{A,ss}/R/T)c^{AC}_{CH_3OH,ss}/c^{ref}_{CH_3OH}(1-\theta_{COx,ss})/(1-\theta^{ref}_{COx})}{s+k^{AD}A_s/V^{AC}+A_s/V^{AC}r_{A10}\exp(\alpha_A F\eta_{A,ss}/R/T)/c^{ref}_{CH_3OH}(1-\theta_{COx,ss})/(1-\theta^{ref}_{COx})} \end{pmatrix}^T \tag{33}$$

$$G_{AT}(s) = \begin{pmatrix} \frac{\alpha_A F/R/T\exp(\alpha_A F\eta_{A,ss}/R/T)/n_{max,Pt}(r_{A10}c^{AC}_{CH_3OH,ss}/c^{ref}_{CH_3OH}(1-\theta_{COx,ss})/(1-\theta^{ref}_{COx})-r_{A20}\theta_{COx,ss}/\theta^{ref}_{COx})}{s-1/n_{max,Pt}(-r_{A10}\exp(\alpha_A F\eta_{A,ss}/R/T)c^{AC}_{CH_3OH,ss}/c^{ref}_{CH_3OH}/(1-\theta^{ref}_{COx,ss})-r_{A20}\exp(\alpha_A F\eta_{A,ss}/R/T)/\theta^{ref}_{COx})} \\ \frac{r_{A10}\exp(\alpha_A F\eta_{A,ss}/R/T)/c^{ref}_{CH_3OH}(1-\theta_{COx,ss})/(1-\theta^{ref}_{COx})/n_{max,Pt}}{s-1/n_{max,Pt}(-r_{A10}\exp(\alpha_A F\eta_{A,ss}/R/T)c^{AC}_{CH_3OH,ss}/c^{ref}_{CH_3OH}/(1-\theta^{ref}_{COx,ss})-r_{A20}\exp(\alpha_A F\eta_{A,ss}/R/T)/\theta^{ref}_{COx})} \end{pmatrix}^T \tag{34}$$

$$G_{AE}(s) = \begin{pmatrix} \frac{-RT(-2r_{A10}\theta^{ref}_{COx}+2r_{A10}\theta^{ref}_{COx}\theta_{COx,ss})}{(2r_{A10}c^{AC}_{CH_3OH,ss}\theta^{ref}_{COx}(\theta_{COx,ss}-1)+r_{A20}\theta_{COx,ss}c^{ref}_{CH_3OH}(\theta^{ref}_{COx,ss}-1))\alpha_A F} \\ \frac{-RT(2r_{A10}c^{AC}_{CH_3OH,ss}\theta^{ref}_{COx}-r_{A20}c^{ref}_{CH_3OH}+r_{A20}c^{ref}_{CH_3OH}\theta^{ref}_{COx})}{(2r_{A10}c^{AC}_{CH_3OH,ss}\theta^{ref}_{COx}(\theta_{COx,ss}-1)+r_{A20}\theta_{COx,ss}c^{ref}_{CH_3OH}(\theta^{ref}_{COx}-1))\alpha_A F} \\ \frac{RT}{\alpha_A F i_{cell,ss}} \end{pmatrix}^T \tag{35}$$

where the anodic charge transfer coefficients are assumed to be identical ($\alpha_A = \alpha_{A1} = \alpha_{A2}$). The overshoot criterion can be derived analogously to the 1*x*-model. All previous parameters are used, except for the reaction rate constants r_{A10} and r_{A20}. The cathodic reaction rate constant of the 1*x*-model, including the assumption of a faster cathodic reaction, is adopted. The criterion for overshoot yields an implicit equation with three variables: r_{A10}, r_{A20} and the initial steady state current density $i_{cell,ss}$. Since this equation is lengthy and complicated, it is not presented here. Furthermore, it cannot be solved explicitly, but can be plotted as a plane in $\mathbb{R}^3$ with an algebraic mathematics program like Maple, as shown in Fig. 12 (top), where $i_{cell,ss}$ is plotted vs. the two reaction constants. The plane separates

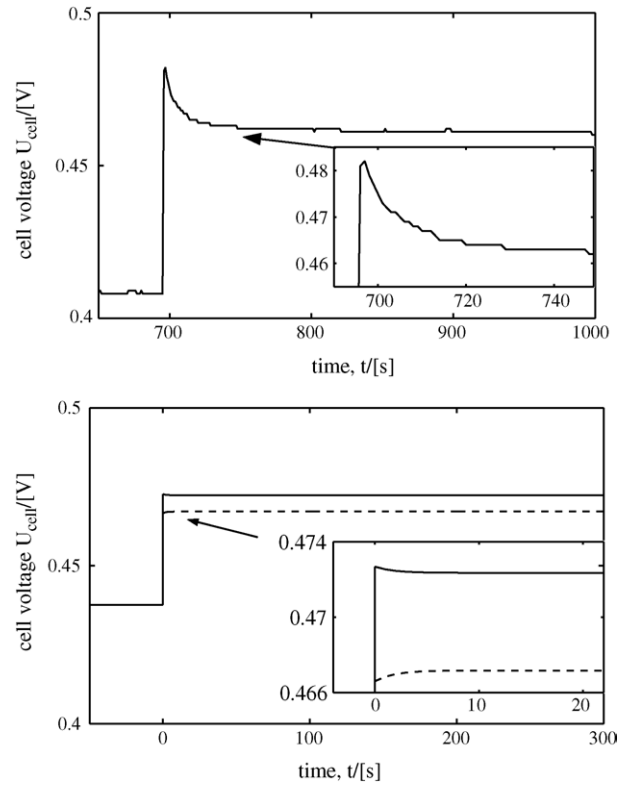

Fig. 11. Experimental voltage response (top) and voltage response of the 1*x*-model (bottom) to a current step from 520 to 260 A m^{-2}: Overshoot response with $\alpha_{A1} = \alpha_C = 0.6$, $r_{A10} = 10^{-7}$ mol m^{-2} s^{-1} (solid), non-overshoot response with $\alpha_{A1} = \alpha_C = 0.5$, $r_{A10} = 1.4 \times 10^{-7}$ mol m^{-2} s^{-1} (dotted).

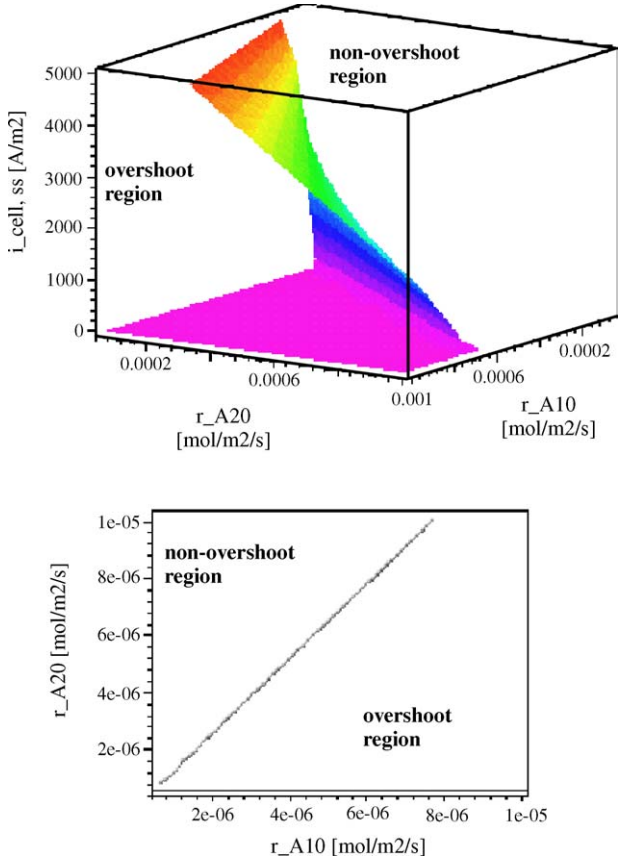

Fig. 12. Analytically calculated separation plane/line between overshooting and non-overshooting region: Anodic reaction constants vs. initial current density (top), anodic reaction constants at initial current density $i_{cell,ss}$ = 520 A m^{-2} (bottom).

the overshoot region (left) from the non-overshoot region (right). It can be seen that the plane shows an incline. At each cell current density, there is a ratio of r_{A10} versus r_{A20} above which overshooting occurs. This ratio is increasing with increasing cell current density. Hence, similar as in the 1*x*-model, for a set of reaction rate constants a maximum current density exists, above which no overshoot can occur.

Such behaviour was not observed in the experiments (see Fig. 5), steps from high initial cell current densities still produce overshoots. Mass transport limitation, which in the models is only accounted for in a simplified form, in the experiments leads to a lower limiting current density. This current density may be lower than the model's maximum current density for overshooting, $i_{cell,max}$, hence according to the model overshoot will always occur. Furthermore, the cell current steps conducted at higher current densities are far from being linear system deflexions (see Section 3.2.6), for which exclusively the model holds.

Fig. 12 (bottom) shows the separation line for the experimental initial current density of 520 A m^{-2}. Here, sets of parameters in the lower right region will result in overshooting behaviour. Due to the experimentally observed overshooting, the anodic reaction parameters should be within the overshooting regime of Fig. 12 (bottom). The anodic reaction parameters are fitted to the experimental polarisation curve, and the dynamic answer to the current density step from 520 to 260 A m^{-2} is simulated. The result is shown in Fig. 13 (parameters are given ibidem or in Nomenclature). While the absolute overshoot is still ten times lower than the experimental one, the relaxation time, approximately 40 s, is close to the experimental relaxation time, indicating more realistic modelling results. A different selection of reaction parameters may lead to higher or lower overshoot, but will not influence the relaxation time. Therefore, a significant step towards a good fit to the experiments is achieved by the 2*x*-model.

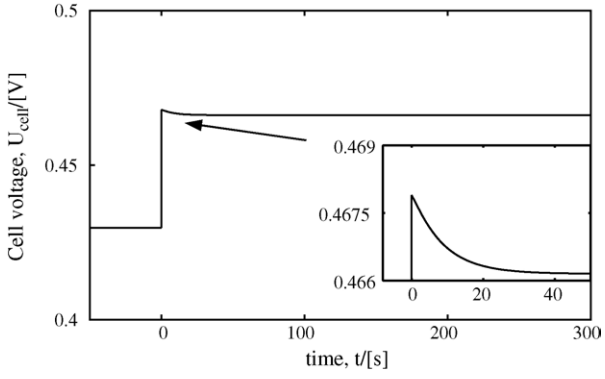

Fig. 13. Voltage response of the 2*x*-model to a current step from 520 to 260 A m^{-2} with $r_{A10} = 10^{-6}$ mol m^{-2} s^{-1}, $r_{A20} = 5 \times 10^{-8}$ mol m^{-2} s^{-1}.

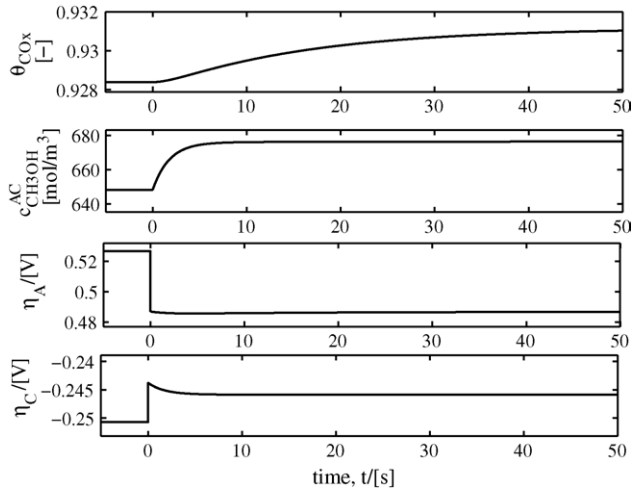

Fig. 14. Concentration and overpotential responses of the non-linear 2*x*-model to a current step from 520 to 260 A m^{-2}. From top to bottom: COx-coverage, methanol concentration in the anode catalyst layer, anodic overpotential, cathodic overpotential.

Fig. 14 shows the result of the simulation of the numerically evaluated non-linear 2*x*-model (see Section 3.2.6). It shows the transient response of θ_{COx}, $c^{\mathrm{AC}}_{\mathrm{CH_3OH}}$, η_{A} and η_{C}. As can be seen, the anodic overpotential η_{A} is quite insensitive to changing concentrations of methanol and to changing COx surface coverages in the anodic catalyst layer for time $t > 0$, while the cathodic overpotential η_{C} shows a significant overshoot which is the reason for the overall cell voltage overshooting. The theoretical result of an insensitivity of the anodic overpotential to changes in methanol concentration has been validated in half-cell measurements on a real fuel cell MEA [22]. As soon as the methanol concentration in the anode catalyst layer reaches a steady state, the methanol flux through the membrane reaches a steady state, and with this also the cathodic overpotential.

This theoretical result supports the interpretation of the experimental observations at the end of Section 3.1 and Fig. 6.

3.2.5. Reaction–adsorption model with two state variables and a distributed membrane (2x + m-model)

The 1*x*-model and the 2*x*-model are focussed on the reaction mechanism and its influence on the dynamic behaviour of the DMFC. The membrane dynamics is neglected there by assuming a steady-state linear concentration profile of methanol in the membrane. But recent studies by Schultz [10] indicate that the concentration profile of methanol in the membrane is not necessarily linear, and the membrane is a significant storage for methanol. To investigate the influence of the dynamics of the membrane on the cell voltage response, the 2*x*-model is extended with a further state variable, which is the local concentration of methanol in the membrane. This model is denoted as $2x + m$-model. Compared to the setup of the previous transfer function elements (G_{C}, $G_{\mathrm{AC}}(s)$, $G_{\mathrm{AT}}(s)$ and G_{AE} of the 2*x*-model hold for this model, too), the setup of the dynamic membrane transfer function element $G_{\mathrm{M}}(s)$ is more complex, since mass transport through the membrane is given by a partial differential equation, see Eqs. (6) and (11). The procedure is as follows. As can be seen in Fig. 9, the input into the membrane module:

$$U_{\mathrm{M}}(s) = \begin{pmatrix} I(s) \\ C^{\mathrm{AC}}_{\mathrm{CH_3OH}}(s) \end{pmatrix} \tag{36}$$

and output out of the membrane

$$Y_{\mathrm{M}}(s) = \begin{pmatrix} N^{\mathrm{M,C}}_{\mathrm{CH_3OH}}(s) \\ d^{\mathrm{M}}/\kappa^{\mathrm{M}} \cdot I(s) \\ N^{\mathrm{M,A}}_{\mathrm{CH_3OH}}(s) \end{pmatrix} \tag{37}$$

are coupled by a 3×2 transfer function matrix $G_{\mathrm{M}}(s)$:

$$Y_{\mathrm{M}}(s) = G_{\mathrm{M}}(s) \cdot U_{\mathrm{M}}(s) \tag{38}$$

with

$$G_{\mathrm{M}}(s) = \begin{pmatrix} G_{\mathrm{M11}}(s) & G_{\mathrm{M12}}(s) \\ d^{\mathrm{M}}/\kappa^{\mathrm{M}} & 0 \\ G_{\mathrm{M31}}(s) & G_{\mathrm{M32}}(s) \end{pmatrix} \tag{39}$$

$G_{\mathrm{M11}}(s)$, $G_{\mathrm{M12}}(s)$, $G_{\mathrm{M31}}(s)$ and $G_{\mathrm{M32}}(s)$ are functions of s and are determined by using Eq. (6), which is linearised at the steady state operating point.

Assuming the following two conditions:

- methanol concentration in the membrane at the spatial coordinate $z = 0$, where the membrane is in contact with the anode catalyst layer, is identical to the concentration in the anode catalyst layer, i.e.

$$c^{\mathrm{M}}_{\mathrm{CH_3OH}}(z = 0) = c^{\mathrm{AC}}_{\mathrm{CH_3OH}}; \tag{40}$$

- methanol concentration in the membrane at $z = d^{\mathrm{M}}$, where the membrane is in contact with the cathode catalyst layer, is assumed to be zero due to the total oxidation of methanol with oxygen, i.e.

$$c^{\mathrm{M}}_{\mathrm{CH_3OH}}(z = d^{\mathrm{M}}) = c^{\mathrm{CC}}_{\mathrm{CH_3OH}} = 0; \tag{41}$$

the following partial differential equation results:

$$\frac{\partial x}{\partial t} = D^{\mathrm{M}}_{\mathrm{CH_3OH}} \frac{\partial^2 x}{\partial z^2} - k_{\phi 2} i_{\mathrm{cell,ss}} \frac{\partial x}{\partial z} + \\ + \frac{{k_{\phi 2}}^2 c^{\mathrm{AC}}_{\mathrm{CH_3OH,ss}} i_{\mathrm{cell,ss}}}{D^{\mathrm{M}}_{\mathrm{CH_3OH}}} \frac{\mathrm{e}^{Pe_{\mathrm{ss}}(z/d^{\mathrm{M}}-1)}}{1 - \mathrm{e}^{-Pe_{\mathrm{ss}}}} (i_{\mathrm{cell}} - i_{\mathrm{cell,ss}}) \tag{42}$$

where the Peclet number:

$$Pe_{\mathrm{ss}} = \frac{k_{\phi 2} d^{\mathrm{M}} i_{\mathrm{cell,ss}}}{D^{\mathrm{M}}_{\mathrm{CH_3OH}}} \tag{43}$$

and the definition $x = (c^{\mathrm{M}}_{\mathrm{CH_3OH}} - c^{\mathrm{M}}_{\mathrm{CH_3OH,ss}})$ and initial condition $x(t=0,z)=0$ are holding, as well as the boundary condition:

$$x(t, z=0) = c^{\mathrm{AC}}_{\mathrm{CH_3OH}} - c^{\mathrm{AC}}_{\mathrm{CH_3OH,ss}}, \qquad x(t, z=d^{\mathrm{M}}) = 0 \tag{44}$$

Laplace transformation yields the following ordinary differential equation:

$$D^{\mathrm{M}}_{\mathrm{CH_3OH}} X''(s,z) - k_{\phi 2} i_{\mathrm{cell,ss}} X'(s,z) - sX(s,z) = -\frac{{k_{\phi 2}}^2 c^{\mathrm{AC}}_{\mathrm{CH_3OH,ss}} i_{\mathrm{cell,ss}}}{D^{\mathrm{M}}_{\mathrm{CH_3OH}}} \frac{\mathrm{e}^{Pe_{\mathrm{ss}}(z/d^{\mathrm{M}}-1)}}{1-\mathrm{e}^{-Pe_{\mathrm{ss}}}} I(s) \tag{45}$$

with $X(s, z=0) = C^{\mathrm{AC}}_{\mathrm{CH_3OH}}(s)$, $X(s, z=d^{\mathrm{M}}) = 0$.

After solving this equation analytically and inserting the result $X(s,z)$ into the Laplace transform of the linearised Eq. (11):

$$N(s,z) = -D^{\mathrm{M}}_{\mathrm{CH_3OH}} X'(s,z) + k_{\phi 2} i_{\mathrm{cell,ss}} X(s,z) + k_{\phi 2} c_{\mathrm{CH_3OH,ss}}(z) I(s) \tag{46}$$

a Laplace transform of the methanol mass flow is obtained, which can be cast into the following form:

$$N(s,z) = b_1(s,z)X(s,z) + b_2(s,z)I(s) \tag{47}$$

b_1 and b_2 are complicated functions of s and z. They are not presented here due to their size.

The transfer function elements demanded in Eq. (39) are obtained from Eq. (47) at the coordinates $z=0$ and $z=d^{\mathrm{M}}$:

$$G_{\mathrm{M11}}(s) = \frac{{k_{\phi 2}}^2 c^{\mathrm{AC}}_{\mathrm{CH_3OH,ss}} i_{\mathrm{cell,ss}}}{2d^{\mathrm{M}}} \frac{\mathrm{e}^{-Pe_{\mathrm{ss}}/2}}{1-\mathrm{e}^{-Pe_{\mathrm{ss}}}} \frac{1}{s} \cdot [-Pe_{\mathrm{ss}}\,\mathrm{e}^{Pe_{\mathrm{ss}}/2} - 2F_1(s) + 2\,\mathrm{e}^{Pe_{\mathrm{ss}}/2} F_2(s)] \tag{48}$$

$$G_{\mathrm{M12}}(s) = \frac{D^{\mathrm{M}}_{\mathrm{CH_3OH}}}{d^{\mathrm{M}}}\,\mathrm{e}^{Pe_{\mathrm{ss}}} F_1(s) \tag{49}$$

$$G_{\mathrm{M31}}(s) = k_{\phi 2} c^{\mathrm{AC}}_{\mathrm{CH_3OH,ss}} - \frac{{k_{\phi 2}}^2 c^{\mathrm{AC}}_{\mathrm{CH_3OH,ss}} i_{\mathrm{cell,ss}}}{2d^{\mathrm{M}}} \frac{\mathrm{e}^{-Pe_{\mathrm{ss}}}}{1-\mathrm{e}^{-Pe_{\mathrm{ss}}}} \frac{1}{s} \cdot [Pe_{\mathrm{ss}} - 2\,\mathrm{e}^{Pe_{\mathrm{ss}}/2} F_1(s) + 2F_2(s)] \tag{50}$$

$$G_{\mathrm{M32}}(s) = -\frac{D^{\mathrm{M}}_{\mathrm{CH_3OH}} Pe_{\mathrm{ss}}}{2d^{\mathrm{M}}} + k_{\phi 2} i_{\mathrm{cell,ss}} + \frac{D^{\mathrm{M}}_{\mathrm{CH_3OH}}}{d^{\mathrm{M}}} F_2(s) \tag{51}$$

with

$$F_1(s) = \frac{\sqrt{(Pe_{\mathrm{ss}}/2)^2 + ((d^{\mathrm{M}})^2/D^{\mathrm{AC}}_{\mathrm{CH_3OH}})s}}{\sinh\sqrt{(Pe_{\mathrm{ss}}/2)^2 + ((d^{\mathrm{M}})^2/D^{\mathrm{AC}}_{\mathrm{CH_3OH}})s}} \tag{52}$$

$$F_2(s) = \frac{\sqrt{(Pe_{\mathrm{ss}}/2)^2 + ((d^{\mathrm{M}})^2/D^{\mathrm{AC}}_{\mathrm{CH_3OH}})s}}{\tanh\sqrt{(Pe_{\mathrm{ss}}/2)^2 + ((d^{\mathrm{M}})^2/D^{\mathrm{AC}}_{\mathrm{CH_3OH}})s}} \tag{53}$$

Unfortunately, these transfer functions are transcendental functions, and using them in this form would not result in a rational transfer function for the fuel cell (Eq. (19)), hence neither can this function be used for controlling purposes nor can an overshoot analysis be carried out according to Eq. (23). There exist several methods to approximate transcendental transfer functions by rational functions, see e.g. [23]. A reliable analytical solution is obtained via a combination of the residue theorem and the Laplace transformation. Step one is the transformation of the inverse Laplace transformation integral into a contour integral with a semicircle of radius $\rho \to \infty$:

$$y(t) = \frac{1}{2\pi j}\int_{c-j\infty}^{c+j\infty} Y(s)\,\mathrm{e}^{st}\mathrm{d}s = \frac{1}{2\pi j}\oint_{\rho\to\infty} Y(s)\,\mathrm{e}^{st}\mathrm{d}s \tag{54}$$

If all singularities of $Y(s)$ are inside this region and if

$$\lim_{s\to\infty} Y(s) = 0 \tag{55}$$

according to the residue theorem the system answer in the time domain $y(t)$ can be calculated by the sum of the contour integrals around each singularity P_i:

$$y(t) = \frac{1}{2\pi j}\oint_{\rho\to\infty} Y(s)\,\mathrm{e}^{st}\mathrm{d}s = \sum_{i=1}^{\infty} \mathrm{res}_i \tag{56}$$

with

$$\mathrm{res}_i = \frac{1}{2\pi j}\oint_{\rho\to 0,\ \text{at } P_i} Y(s)\,\mathrm{e}^{st}\mathrm{d}s \tag{57}$$

Integration of this equation yields:

$$\mathrm{res}_i = \lim_{s\to P_i}(s-P_i)Y(s)\,\mathrm{e}^{st} = \mathrm{const}\,\mathrm{e}^{P_i\cdot t} \tag{58}$$

Since the Laplace transform of $\mathrm{e}^{P_i\cdot t}$ is $\frac{1}{s-P_i}$, $y(t)$ can be transformed into the Laplace domain, resulting in the following rational form of the transfer function:

$$Y_{\mathrm{rat}}(s) = \sum_{i=1}^{\infty}\left(\lim_{s\to P_i}(s-P_i)Y(s)\right)\frac{1}{s-P_i} \tag{59}$$

For functions with an infinite number of singularities, the higher terms represent faster dynamic modes ($\leq$ milliseconds) and more negative singularities P_i. These become irrelevant for the contemplated order of magnitude of experimental relaxation times (seconds–minutes). Since the transfer function should have the same stationary gain as $Y(s)$, i.e. $Y(0)$ according to the final value theorem, the sum in Eq. (59) is convergent for $s=0$. Therefore, a good approximation can be achieved by truncating the series after the time-relevant m terms, i.e. time-relevant m singularities, and correcting for the stationary gain:

$$Y(s) \approx Y_{rat}(s) - Y_{rat}(0) + Y(0) \tag{60}$$

This rationalising procedure is applied to the transcendental parts F_1 (Eq. (52)) and F_2 (Eq. (53)) of the transfer functions,

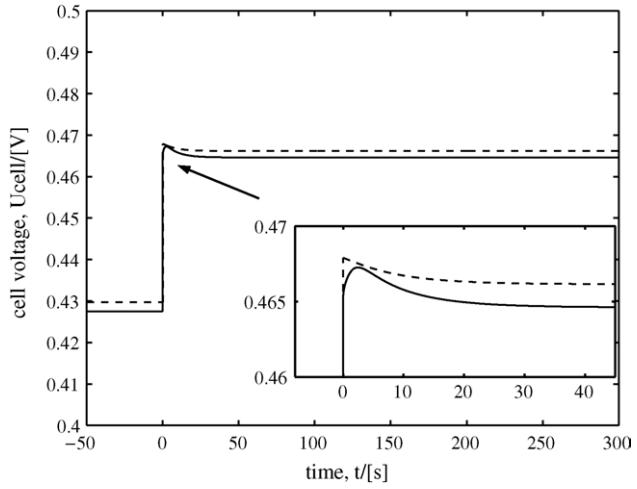

Fig. 15. Comparison of voltage responses of the $2x + m$-model (solid) and the $2x$-model (dashed) to a current step from 520 to 260 A m^{-2} with $r_{A10} = 10^{-6}$ mol m^{-2} s^{-1}, $r_{A20} = 5 \times 10^{-8}$ mol m^{-2} s^{-1}.

$G_{M11}(s)$–$G_{M32}(s)$:

$$F_1(s) \rightarrow F_{1,\mathrm{rat}} = \sum_{i=1}^{m} \left(\lim_{s \rightarrow P_i} (-1)^{k+1} \frac{(Pe_{ss}/2)^2 + k^2\pi^2}{(d^M)^2 / D^{AC}_{CH_3OH}} \right) \frac{1}{s - P_i} \quad (61)$$

$$F_2(s) \rightarrow F_{2,\mathrm{rat}} = \sum_{i=1}^{m} \left(\lim_{s \rightarrow P_i} -\frac{(Pe_{ss}/2)^2 + k^2\pi^2}{(d^M)^2 / D^{AC}_{CH_3OH}} \right) \frac{1}{s - P_i} \quad (62)$$

$F_2(s)$ does not fulfill the condition in Eq. (55), but $F_{2,\mathrm{rat}}$ is still an adequate fit to the original function, as can be shown.

The new transfer functions are inserted into the block diagram (Fig. 9), and the cell voltage response to the experimental current step is simulated. The reaction parameters are identical to these of the $2x$-model, as well as most of the other parameters (values see Nomenclature). The results are displayed in Fig. 15 in comparison to the voltage response of the $2x$-model. As can be seen, the relaxation time is identical to that of the $2x$-model. Observed differences are a 2 s delay time until the maximum voltage is reached (discussion see next paragraph), and a lower steady state of the $2x + m$-model. The absolute overshoot is slightly larger than for the $2x$-model, but it is still small compared to the experimental voltage response, whose overshoot is 10 times larger. Hence, for the given parameter set and with regard to the experiment, the results of the $2x$-model and the $2x + m$-model are qualitatively equal.

Observing concentration and overpotential changes of the numerically evaluated nonlinear $2x + m$-model in Fig. 16 (see Section 3.2.6), we see the same effect as in the $2x$-model: methanol concentration dominates the dynamics of the cathodic overpotential, and thus the cell voltage. Even after 50 s, the COx coverage is not in equilibrium.

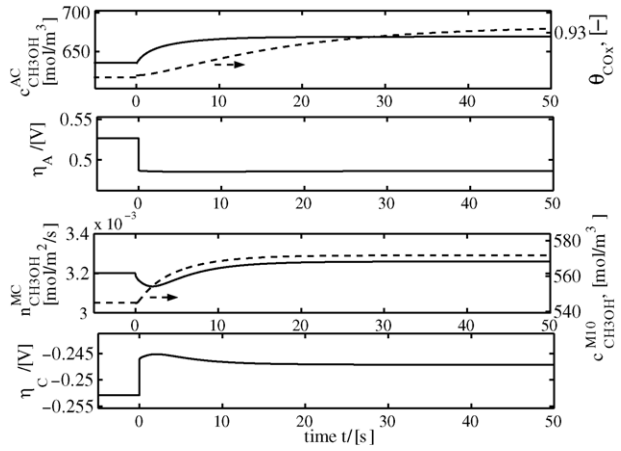

Fig. 16. Concentrations and overpotential responses of the nonlinear $2x + m$-model to a current step from 520 to 260 A m^{-2}. From top to bottom: Methanol concentration and surface coverage in the anode catalyst layer, anodic overpotential, methanol flux at the interface membrane/cathodic catalyst layer and methanol concentration in the membrane (10th discretisation element of 50 elements in total), cathodic overpotential.

The dynamic behaviour of the flux at the interface membrane/cathode shows the effect of the introduced osmotic drag term: methanol flux instantaneously decreases at $t = 0$ due to the reduced current density, hence due to lower osmotic drag, while subsequently the anodic methanol concentration increases, causing a rise in the flux. This non-minimal phase behaviour leads to an overshooting of the cathodic overpotential response and, as a consequence, the above presented overall cell voltage response (see Fig. 15) also overshoots. Just like in the $2x$-model, the anodic overpotential is quite insensitive to changes in the methanol feed concentration and surface coverage.

3.2.6. Discussion on validity of transfer function models

The last two sections presented dynamic responses of the $2x$-model and the $2x + m$-model. The responses were obtained by linearising the rigorous model equations around the steady state and calculating the voltage transient to a current step, using Laplace transformation. As can be seen from the results, the models can describe the observed experimental behaviour qualitatively, but not quantitatively.

Between the current densities of 520 and 260 A m^{-2}, the experimental polarisation curve is approximately linear (see Fig. 2), and hence the system could be regarded as a linear one. This will be shown in the following.

For comparison with the linearised transfer function models, the nonlinear system answers to the $2x$-model and the $2x + m$-model have been calculated by numerical solving of the respective set of nonlinear differential equations (see also Figs. 14 and 16). Both, the nonlinear and linear system answers are presented in Fig. 17 (top) for comparison. As can be seen for both, the $2x$-model and the $2x + m$-model, voltage responses of the linearised and nonlinear systems have the same shape except that the nonlinear answer is shifted to higher voltages. This shift is due to the deviation of the

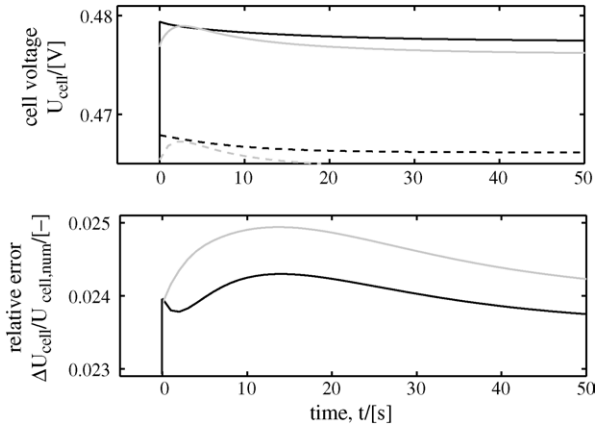

Fig. 17. Comparison of linear models with non-linear models. (Top) Voltage response of non-linear models ($2x$: solid black; $2x+m$: solid grey) and transfer function models ($2x$: dashed black; $2x+m$: dashed grey). (Bottom) Relative error of linear compared to non-linear responses of the $2x$-model (black) and the $2x+m$-model (grey).

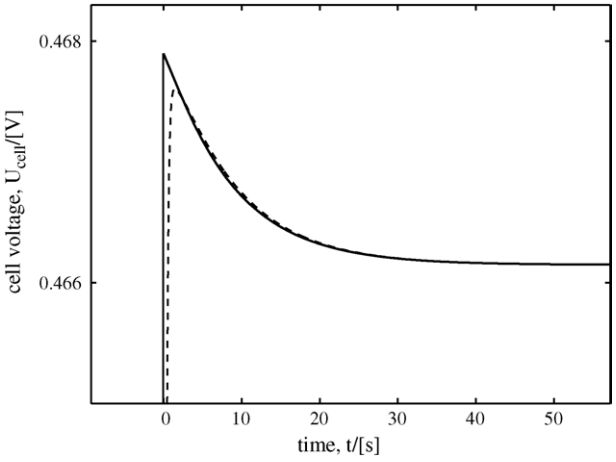

Fig. 18. Voltage response of the $2x$-model (solid) and $4x$-model (dashed) to a current step from 520 to 260 A m^{-2} with $r_{A10} = 10^{-6}$ mol m^{-2} s^{-1}, $r_{A20} = 5 \times 10^{-8}$ mol m^{-2} s^{-1}.

polarisation curve from the tangent of the polarisation curve at the initial current density. A quantitative analysis of the deviation is given in Fig. 17 (bottom), where the relative errors of the linear models vs. the nonlinear models are plotted. It can be seen for the $2x$-model that the relative error in the steady state is quite small (2.4%). Even less, approximately 0.02%, is the change of this error versus time. Therefore, it can be concluded that the linearised $2x$-model is equivalent to the nonlinear $2x$-model for the given current step. This may change with increasing current step size where the deviation from the polarisation curve will increase. The relative error of the linearised $2x+m$-model is only slightly higher ($\approx$2.4%), and the variance of the error is in the same order as for the $2x$-model. Hence, also for the $2x+m$-model, it can be concluded that it is equivalent to its non-linear counterpart.

3.2.7. Reaction–adsorption-charge model with four state variables (4x-model)

In all models presented in the previous sections, it was assumed that the time constants of the charge balances are much smaller than the time constants of the mass balances, which means that the charge balances are in equilibrium instantaneously, i.e. in a quasi-steady state. This assumption seems justified, since in the experiments the Ohmic part of the voltage change ($R^{M} \cdot \Delta i_{cell} = 3$ mV) is only a small part of the total steady-state voltage change (=52 mV) for the standard current density step, i.e. from 520 to 260 A m^{-2}.

Nonetheless, if the given set of equations (Eqs. (3)–(12)) and parameters (see Nomenclature) are reliable, a model including the dynamics of the charge balances should deviate only marginally from the $2x$-model. In the following, it will be shown how the system dynamics changes when the dynamics of charge balances is not neglected. Additionally to the two state variables $c^{AC}_{CH_3OH}$ and θ_{COx} of the $2x$-model, the state variables η_A and η_C, are described by dynamic balances (charge balances, Eqs. (5) and (7)). The model now consists of four state variables, subsequently it is denoted as $4x$-model. The total transfer function is modified by exchanging the transfer function elements G_{AE} and G_C in the blockdiagram (see Fig. 9):

$$G_C(s) = \begin{pmatrix} -\dfrac{1/C^{CC}}{s - 6/C^{CC}F^2 r_{C0}(\alpha_C - 1)/R/T \exp((\alpha_C - 1)F/R/T\eta_{C,ss})} \\ \dfrac{-6F/C^{CC}}{s - 6/C^{CC}F^2 r_{C0}(\alpha_C - 1)/R/T \exp((\alpha_C - 1)F/R/T\eta_{C,ss})} \end{pmatrix}^{T} \tag{63}$$

$$G_{AE}(s) = \begin{pmatrix} \dfrac{-4Fr_{A10}\exp(\alpha_A F\eta_{A,ss}/R/T)/c^{ref}_{CH_3OH}(1-\theta_{COx,ss})/(1-\theta^{ref}_{COx})/C^{AC}}{s - \alpha_A/R/T\exp(\alpha_A F\eta_{A,ss}/R/T)/C^{AC}(-4F^2 r_{A10}c^{AC}_{CH_3OH,ss}/c^{ref}_{CH_3OH}(1-\theta_{COx,ss})/(1-\theta^{ref}_{COx}) - 2F^2 r_{A20}\theta_{COx,ss}/\theta^{ref}_{COx})} \\ \dfrac{(4Fr_{A10}\exp(\alpha_A F\eta_{A,ss}/R/T)c^{AC}_{CH_3OH,ss}/c^{ref}_{CH_3OH}/(1-\theta^{ref}_{COx}) - 2Fr_{A20}\exp(\alpha_A F\eta_{A,ss}/R/T)/\theta^{ref}_{COx})/C^{AC}}{s - \alpha_A/R/T\exp(\alpha_A F\eta_{A,ss}/R/T)/C^{AC}(-4F^2 r_{A10}c^{AC}_{CH_3OH,ss}/c^{ref}_{CH_3OH}(1-\theta_{COx,ss})/(1-\theta^{ref}_{COx}) - 2F^2 r_{A20}\theta_{COx,ss}/\theta^{ref}_{COx})} \\ \dfrac{1/C^{AC}}{s - \alpha_A/R/T\exp(\alpha_A F\eta_{A,ss}/R/T)/C^{AC}(-4F^2 r_{A10}c^{AC}_{CH_3OH,ss}/c^{ref}_{CH_3OH}(1-\theta_{COx,ss})/(1-\theta^{ref}_{COx}) - 2F^2 r_{A20}\theta_{COx,ss}/\theta^{ref}_{COx})} \end{pmatrix}^{T} \tag{64}$$

Using the same set of parameters as in the $2x$-model, the dynamic voltage response is calculated for the current density step from 520 to 260 A m^{-2}. The voltage response of both, $2x$- and $4x$-model, is shown in Fig. 18. As can be seen, the time for reaching the new steady state is the same in both models. Five seconds after the current step both answers are identical. But, as expected, there is a slight discrepancy in the domain of the small time constants, i.e. in the first 3 s. In

the 4*x*-model, the voltage cannot step-up immediately to the new level at $t \rightarrow 0^+$, as it is found for the 2*x*-model, since the double layers first have to be discharged. This discharge takes place within three seconds, after which the voltage reaches its maximum. In the subsequent time only small voltage changes due to concentration changes are observed, compared to the initial large voltage changes due to the current step, and the voltage decreases slowly. As a result, comparing the absolute overshoots of the 2*x*-model and 4*x*-model, the overshoot of the 4*x*-model is 15% smaller than that of the 2*x*-model. Nonetheless, one has to take into account that the voltage response will always show this characteristic rounding off of the overshoot within the first few seconds (time depends on the double layer capacities), but the 4*x*-model will not contribute other dynamic effects to the system. Finally, the previously postulated assumption that the 4*x*-model deviates only marginally from the 2*x*-model proved correct, the set of equations showed the predicted behaviour, and for the sake of model reduction, the models with quasi-steady state charge balances may be used for modelling further on.

4. Conclusions

This work presented investigations on the dynamic behaviour of the DMFC. Experimental cell voltage responses to load step changes were investigated based on a transfer function approach. The here presented models hold for analysis of a specific operating regime (low anodic residence time ($\sim$1 s), low current densities), in which dynamic processes occurring inside the MEA are minimally influenced by mass transport phenomena (CO_2 bubble generation, concentration distribution in anode compartment).

Applying cell current steps to the DMFC, the voltage response in most cases showed significant overshooting behaviour. The height of overshooting strongly varied depending on the position of the investigated steady state of the DMFC at the polarisation curve, hence on the dominating physico-chemical phenomena in different operating regimes. Switching to OCV caused overshoots of 80%. Understanding such dynamic effects is not only essential for DMFC operation, but also for understanding the processes occurring inside the cell.

Linear system analysis was applied to a set of dynamic models with different complexity. A criterion for cell voltage overshooting was developed, with which parameter domains for overshooting were analytically determined. Although even a model with only one state variable (i.e. methanol concentration in the anode catalyst layer) is able to generate cell voltage overshooting, a much better accordance with the experiments was achieved when introducing a consecutive reaction mechanism and thus working with two state variables: the methanol concentration and the COx surface coverage in the anode catalyst layer. The implementation of additional dynamic state variables (methanol concentration in the membrane, cathodic and anodic overpotentials), for the given parameter set, led to only slightly different results. In all investigated model variants, the dominating physico-chemical phenomena were the same: Transport of methanol through the membrane caused cathodic overpotential overshooting while the anodic overpotential proved to be rather insensitive to methanol concentration changes.

Linearised models were found to be adequate for dynamic modelling in the lower pseudo-ohmic regime of the steady-state polarisation curve at high anode flow rates, hence they also could be suitable for controller design for this regime, which will be the scope of future works. Furthermore, the causes of the observed overshoot height, which could not yet be reproduced quantitatively by the presented models, will be investigated (more realistic anode and cathode kinetics).

The transfer function library enabled the modular combination of descriptions of physico-chemical phenomena inside the MEA of the DMFC. Further investigations will be conducted by enlarging the library with modules describing outer mass transport. Finally, the transfer function library will be used for EIS simulations.

Acknowledgements

The authors thank Dipl.-Ing. Deyan Naydenov for experimental support and cand.-Ing. Christian Borchert for support in data postprocessing.

References

[1] J. Kallo, J. Kamara, W. Lehnert, R. von Helmolt, Cell voltage transients of a gas-fed direct methanol fuel cell, J. Power Sources 127 (2004) 181–186.
[2] A. Simoglou, P. Argyropoulos, E. Martin, K. Scott, A. Morris, W. Taama, Dynamic modelling of the voltage response of direct methanol fuel cells and stacks. Part I. Model development and validation, Chem. Eng. Sci. 56 (2001) 6761–6772.
[3] P. Argyropoulos, K. Scott, W. Taama, Dynamic response of the direct methanol fuel cell under variable load conditions, J. Power Sources 87 (2000) 153–161.
[4] P. Argyropoulos, K. Scott, W. Taama, The effect of operating conditions on the dynamic response of the direct methanol fuel cell, Electrochim. Acta 45 (2000) 1983–1998.
[5] P. Heidebrecht, K. Sundmacher, Dynamic modeling and simulation of a countercurrent molten carbonate fuel cell (MCFC) with internal reforming, Fuel Cells 2 (3–4) (2002) 166–180.
[6] M. Ceraolo, C. Miulli, A. Pozio, Modelling static and dynamic behaviour of proton exchange membrane fuel cells on the basis of electrochemical description, J. Power Sources 113 (2003) 131–144.
[7] K. Sundmacher, T. Schultz, S. Zhou, K. Scott, M. Ginkel, E. Gilles, Dynamics of the direct methanol fuel cell (DMFC): experiments and model-based analysis, Chem. Eng. Sci. 56 (2001) 333–341.
[8] S. Yerramalla, A. Davari, A. Feliachi, T. Biswas, Modeling and simulation of the dynamic behavior of a polymer electrolyte fuel cell, J. Power Sources 124 (2003) 104–113.
[9] S. Zhou, T. Schultz, M. Peglow, K. Sundmacher, Analysis of the nonlinear dynamics of a direct methanol fuel cell, Phys. Chem. Chem. Phys. 3 (2001) 347–355.

[10] T. Schultz, Experimental and model-based analysis of the steady-state and dynamic operating behaviour of the direct methanol fuel cell (DMFC), PhD Thesis, University of Magdeburg, Germany, 2005.
[11] V. Gogel, T. Frey, Z. Yongsheng, K. Friedrich, L. Joerissen, J. Garche, Performance and methanol permeation of direct methanol fuel cells: dependence on operating conditions and on electrode structure, J. Power Sources 127 (2004) 172–180.
[12] A. Siebke, W. Schnurnberger, F. Meier, G. Eigenberger, Investigation of the limiting processes of a DMFC by mathematical modeling, Fuel Cells 3 (1–2) (2003) 37–47.
[13] H. Gasteiger, N. Markovic, P. Ross, E. Cairns, Temperature-dependent methanol electro-oxidation on well-characterized Pt–Ru alloys, J. Electrochem. Soc. 141 (7) (1994) 1795–1803.
[14] T. Schultz, K. Sundmacher, Rigorous dynamic model of a direct methanol fuel cell based on Maxwell–Stefan mass transport equations and a Flory–Huggins activity model: Formulation and experimental validation, J. Power Sources, 145 (2005) 435–462.
[15] V. Bagotzky, Y. Vassiliev, O.A. Khazova, Generalized scheme of chemisorption, electrooxidation and electroreduction of simple organic compounds on platinum group metals, J. Electroanal. Chem. 81 (1977) 229–238.
[16] J. Leger, Mechanistic aspects of methanol oxidation on Pt-based electrocatalysts, J. Appl. Electrochem. 31 (2001) 767–771.
[17] H. Wang, C. Wingender, H. Baltruschat, M. Lopez, M.T. Reetz, Methanol oxidation on Pt, PtRu, and colloidal Pt electrocatalysts: a DEMS study of product formation, J. Electroanal. Chem. 509 (2001) 163–169.
[18] A. Kabbabi, R. Faure, R. Durand, B. Beden, F. Hahn, J.M. Leger, C. Lamy, In situ FTIRS study of the electrocatalytic oxidation of carbon monoxide and methanol at Pt–Ru bulk alloy electrodes, J. Electroanal. Chem. 444 (1998) 41–53.
[19] A. Arico, P. Creti, H. Kim, R. Mantegna, N. Giordano, V. Antonucci, Analysis of the electrochemical characteristics of a DMFC based on Pt–Ru/C anode catalyst, J. Electrochem. Soc. 143 (12) (1996) 3950–3959.
[20] S.L. Gojkovic, T.R. Vidakovic, D.R. Djurovic, Kinetic study of methanol oxidation on carbon-supported PtRu electrocatalyst, Electrochim. Acta 48 (2003) 3607–3614.
[21] R. Schloegl, Membrane permeation in systems far from equilibrium, Berichte der Bunsengesellschaft fuer Physikalische Chemie 70 (1966) 400–414.
[22] T. Vidakovic, M. Christov, K. Sundmacher, Rate expression for electrochemical oxidation of methanol on a direct methanol fuel cell anode, J. Electroanal. Chem. 580 (2005) 105–121.
[23] T. Wik, On modelling the dynamics of fixed biofilm reactors, PhD Thesis, Chalmers University of Technology, Goeteborg, Sweden, 1999.
[24] R. Reid, J. Prausnitz, B. Polling, The Properties of Gases and Liquids, 4th ed., McGraw-Hill, New York, 1987.
[25] D. Bernardi, M. Verbrugge, Mathematical model of a gas-diffusion electrode bonded to a polymer electrolyte, AIChE J. 37 (8) (1991) 1151–1163.